Vietnam Journal of Earth Sciences, 46(3), 432-448, https://doi.org/10.15625/2615-9783/21009

Vietnam Journal of Earth Sciences
https://vjs.ac.vn/index.php/jse

Reliable Euler deconvolution solutions of gravity data throughout the β-VDR and THGED methods: Application to mineral exploration and geological structural mapping

Luan Thanh Pham[1*], Saulo Pomponet Oliveira[2], Minh Le-Huy[3], Dat Viet Nguyen[1], Trang Quynh Nguyen-Dang[1], Thanh Duc Do[1], Kha Van Tran[4], Hong-Duyen Thi Nguyen[1], To-Nhu Thi Ngo[1], Hung Quang Pham[5,6]

[1]*University of Science, Vietnam National University, Hanoi, Vietnam*
[2]*Department of Mathematics and Graduate Program in Geology, Federal University of Parana', Curitiba, PR, Brazil*
[3]*Institute of Geophysics, Vietnam Academy of Science and Technology, Hanoi, Vietnam*
[4]*Institute of Marine Geology and Geophysics, Vietnam Academy of Science and Technology, Hanoi, Vietnam*
[5]*Geophysics Department, Hanoi University of Mining and Geology, Hanoi, Vietnam*
[6]*Union of Geophysics, Hanoi, Vietnam*

Received 05 April 2024; Received in revised form 10 May 2024; Accepted 23 May 2024

ABSTRACT

Euler deconvolution (ED) is mainly used to estimate the locations and depths of magnetic bodies. This technique can also be applied to gravity anomalies but requires caution, as Euler solutions directly obtained from gravity anomalies may provide misleading results. In addition, the traditional Euler deconvolution generates many spurious solutions and is noise-sensitive. This research presents an improved method for the ED of gravity anomalies. This method is based on a finite-difference method (β-VDR) that provides robust vertical derivatives of gravity anomalies, and the total horizontal gradient-based edge detection method (THGED) used to select the Euler solutions, filtering out spurious solutions. Our method is exemplified with two synthetic gravity models and two real datasets from the Voisey's Bay deposit (Canada) and the Hanoi basin (Vietnam). The advantage of the proposed method is that it can provide the depths more accurately and is less sensitive to noise than some modified ED methods.

Keywords: Edge detection, stable finite difference, gravity data, Euler deconvolution.

1. Introduction

Euler deconvolution (ED) is one of the most popular quantitative interpretation methods for magnetic anomalies (Florio et al., 2006). The horizontal location and depth of sources are obtained from the ED without an assumption on magnetization intensity (Ekinci et al., 2014). The ED was introduced by Thompson (1982) for 2D sources and extended for 3D sources by Reid et al. (1990). The popularization of the ED is mainly due to its incredible simplicity of implementation and use, providing an excellent choice for a rapid initial interpretation. The ED has successfully outlined contacts, faults, trends, tectonic blocks, and basements from magnetic

---

*Corresponding author, Email: luanpt@hus.edu.vn data (Zhang et al., 2015). Some comprehensive estimations of this technique are presented by Jekeli (2009), Reid et al. (2014), and Pašteka and Kušnirák (2020).

The ED involves passing a user-defined window over the grid, and the depth of sources is computed by solving linear least-squares problems within windows. Since this method scans the whole data to obtain the depths, it typically produces many false solutions (Catalán and Martín Davila, 2003; Castro et al., 2020). Spurious solutions may also result from noise in the field, which is amplified when derivatives of the field are computed (Cooper, 2004; Pašteka and Richter, 2005). Some criteria have been introduced to constrain solutions. Thompson (1982) proposed using a tolerance value to remove normalized depth solutions smaller than this value. Barbosa et al. (1999) suggested an acceptance criterion that removes solutions with residual norms less than a specified maximum. Chen et al. (2014) proposed retaining only highly clustered solutions. An alternative approach taking advantage of edge filters (Pal et al., 2016a, b; Narayan et al., 2016; 2021; Nasuti et al., 2019; Sahoo et al., 2022a, b; Jorge et al., 2023; Pham and Prasad, 2023; Alvandi and Ardestani, 2023; Alvandi and Ghanati, 2023; Oliveira et al., 2023; Pham 2023, 2024a, b, c; Kafadar and Oksum, 2024) is to compute ED inside areas determined by source edge locations, for example, the total horizontal gradient (ED-THG) (Fairhead et al., 1994; Huang et al., 2022), total gradient (ED-TG) (Catalán and Martín Davila, 2003; Ruppel et al., 2018), normalized total horizontal gradient (Alamdar et al., 2015), combined tilt derivative filters (Castro et al., 2018; 2020), and enhanced total horizontal gradient (Pham et al., 2024a).

The ED has been extended to gravity sources (e.g., Marson and Klingele, 1993; Zhang et al., 2000; Reid et al., 2003; Son et al., 2005; Beiki, 2010) and has been applied to interpret gravity anomalies in some geological scenarios (Saadi et al., 2008; Kumar et al., 2020; Ganguli et al., 2021; Aprina e al., 2024). Unlike magnetic data, the ED is routinely applied to the vertical derivative of gravity anomalies. This technique has also been applied to gravity anomalies (El Gout, 2010; Kumar et al., 2018, 2022; EL-Badrawy et al., 2021; Melouah et al., 2023). The latter approach may be pursued by a suitable modification of the structural index, but it leads to theoretical difficulties in the case of the contact model (Reid et al., 2003).

In this study, we review the ED for the gravity case and propose an improved version (ED-THGED) where we constrain its solutions by using moving windows determined by the peaks of THGED, a total horizontal gradient-based edge detection method (Pham et al., 2024b). We also use a stable vertical derivative calculation method (Oliveira and Pham, 2022) to reduce spurious solutions. The efficacy of the proposed algorithm is exemplified with two gravity models and two real datasets from the Voisey's Bay deposit (Canada) and the Hanoi basin (Vietnam).

2. Methodology

The locations of geological structures can be estimated from their magnetic anomalies using the ED (Thompson, 1982; Reid et al., 1990). This algorithm finds magnetic source locations (x_0, y_0, z_0), which we refer to as solutions by solving a least-squares system given by Euler's homogeneity equation,

$$(x - x_0)\frac{\partial \Delta T}{\partial x} + (y - y_0)\frac{\partial \Delta T}{\partial y} + (z - z_0)\frac{\partial \Delta T}{\partial z} = -N\Delta T \tag{1}$$

over the point (x, y, z) of a moving window that scans the entire grid.

The operators $\partial\Delta T/\partial$x, $\partial\Delta T/\partial$y, and $\partial\Delta T/\partial$z denote derivatives in the *x*, *y,* and *z* directions. Moreover, *N* denotes the structural index, which identifies the source geometry.

For the gravity case, the magnetic data ΔT is replaced by the vertical derivative of the gravity anomaly $\partial\Delta$g/∂z (Marson and Klingele, 1993), i.e.,

$$(x - x_0)\frac{\partial^2 \Delta g}{\partial z \partial x} + (y - y_0)\frac{\partial^2 \Delta g}{\partial z \partial y} + (z - z_0)\frac{\partial^2 \Delta g}{\partial z^2} = -N\frac{\partial \Delta g}{\partial z}, \tag{2}$$

where $\partial\Delta$g/∂z is calculated using the β-VDR method, balancing accuracy and stability. According to Oliveira and Pham (2022), the vertical derivative $\partial\Delta$g/∂z is given by:

$$\frac{\partial \Delta g}{\partial z} = \frac{c_1\Delta g(h_1) + c_2\Delta g(h_2) + c_3\Delta g(h_3) + c_4\Delta g(h_4) + c_5\Delta g(h_5)}{\Delta h} \tag{3}$$

with c_1, ..., c_5 are given by:

$$\begin{cases} c_1 = (2\beta^3 + 15\beta^2 + 35\beta + 25)/12\,, \\ c_2 = (-8\beta^3 - 54\beta^2 - 104\beta - 48)/12\,, \\ c_3 = (12\beta^3 + 72\beta^2 + 114\beta + 36)/12\,, \\ c_4 = (-8\beta^3 - 42\beta^2 - 56\beta - 16)/12\,, \\ c_5 = (2\beta^3 + 9\beta^2 + 11\beta + 3)/12, \end{cases} \tag{4}$$

and $\Delta g(h_i)$ is an upward continuation anomaly at $h_i = -\beta\Delta h - (i-1)\Delta h$, Δh is the spacing increment, and β is the stabilizing parameter. We can use Δh = 1/100 or 1/10 of grid spacing (Oliveira and Pham, 2022; Pham et al. (2024a), while β is between 20 and 60 (Oliveira and Pham, 2022; Pham, 2024b).

The horizontal derivatives of $\partial\Delta$g/∂z in Eq (2) are calculated by standard finite differences (Ekinci and Yiğitbaş, 2012, 2015), while the Laplace equation is used to obtain the second-order vertical derivative,

$$\frac{\partial^2 \Delta g}{\partial z^2} = -\frac{\partial^2 \Delta g}{\partial x^2} - \frac{\partial^2 \Delta g}{\partial y^2}. \tag{5}$$

As well known from the literature, the ED algorithm usually generates many spurious solutions, and one or more strategies are usually employed to filter them out (FitzGerald et al., 2004). Herein, we adopt the following strategies:

- ✓ Negative depth values are discarded;
- ✓ Isolated solutions are discarded;
- ✓ The moving window is restricted to a few grid points.

We regard a solution as isolated if its distance from the other solutions is more significant than a prescribed value d_{min}. Moreover, we designed a constraining mask with points that serve as the centers of the moving windows (Castro et al., 2020). This mask is composed of all grid points such that *THGED* > *tol*, where *tol* is a prescribed tolerance, and *THGED* is the following edge-detection filter (Pham et al., 2024b):

$$THGED = atan\frac{\frac{\partial THG}{\partial z} - \sqrt{\left(\frac{\partial THG}{\partial x}\right)^2 + \left(\frac{\partial THG}{\partial y}\right)^2}}{\sqrt{\left(\frac{\partial THG}{\partial x}\right)^2 + \left(\frac{\partial THG}{\partial y}\right)^2 + \left(\frac{\partial THG}{\partial z}\right)^2}}, \tag{6}$$

where THG is given by (Cordell, 1979):

$$THG = \sqrt{\left(\frac{\partial \Delta g}{\partial x}\right)^2 + \left(\frac{\partial \Delta g}{\partial y}\right)^2}. \qquad (7)$$

3. Results

The effectiveness of the proposed method (ED-THGED) is demonstrated with two synthetic models and two field datasets from the Voisey's Bay deposit (Canada) and Hanoi basin (Vietnam). The ED-THGED was performed using windows with a popular size of 10×10 observation points (Castro et al., 2020) and a structural index of 0 for contacts, as Marson and Klingele (1993) recommended. In this study, we used $\Delta h =$ 0.1 of grid spacing and β = 40 for all examples. The results of the ED-THGED are also compared to those of the improved Euler deconvolution versions based on the total horizontal gradient (ED-THG) and total gradient (ED-TG) with THG is given by Eq. (7) and TG is defined by (Roest et al., 1992; Ekinci et al., 2013):

$$TG = \sqrt{\left(\frac{\partial \Delta g}{\partial x}\right)^2 + \left(\frac{\partial \Delta g}{\partial y}\right)^2 + \left(\frac{\partial \Delta g}{\partial z}\right)^2}. \qquad (8)$$

Like the THG and THGED, the TG uses maxima to outline the edges. The ED-THG and ED-TG also discarded isolated solutions and solutions where $THG < \frac{\max(THG)}{100}$ or $TG < \frac{\max(TG)}{100}$.

3.1. Theoretical examples

The first model includes a prismatic source with a 100 kg/m^3 density contrast. The prism is 300 × 300 m^2 with a depth of 30 m. Figs. 1a and 1b show the model and its gravity anomaly. Figs. 2a-c show the THG, TG, and THGED of the anomaly, respectively. We can see that the peaks in the THG and THGED maps are positioned close to the actual edges, while the peaks of the TG are not. The locations of these THG and TG peaks are obtained using the Blakely and Simpson (1986) method and are then used for the ED-THG and ED-TG methods. As the THGED is a normalization detector, we used the locations of the values greater than or equal to 0.3 for the presented technique ED-THGED (i.e., *tol*=0.3). Figs. 2d-f depict the depths from applying the ED-THG, ED-TG, and ED-THGED, respectively. The histograms of these depths are shown in Figs. 2g-i, respectively. The average depths in Figs. 2d-f are 29.1, 11, and 29.5 m, respectively. The ED-THGEDs bring better depth estimates than the ED-THG and ED-TG.

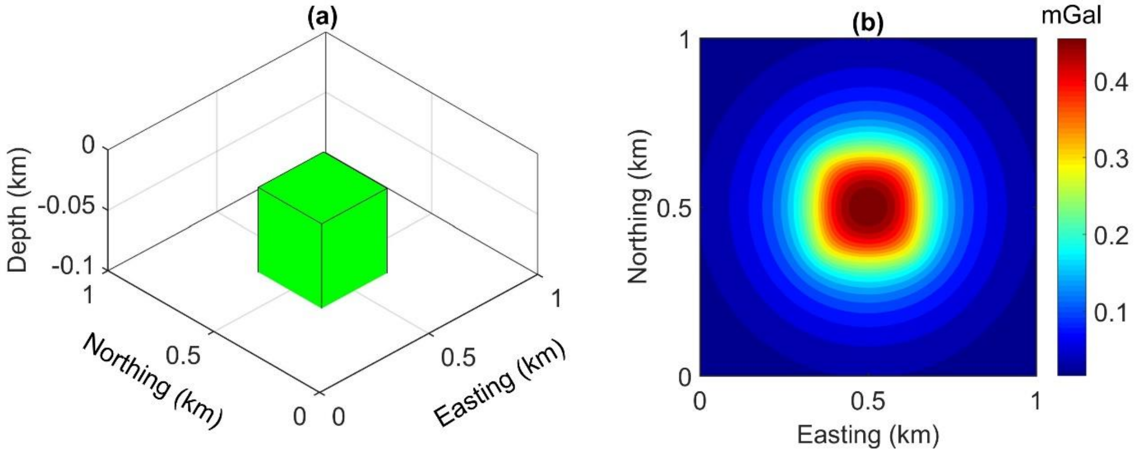

Figure 1. (a) The first model, (b) gravity anomaly of the model

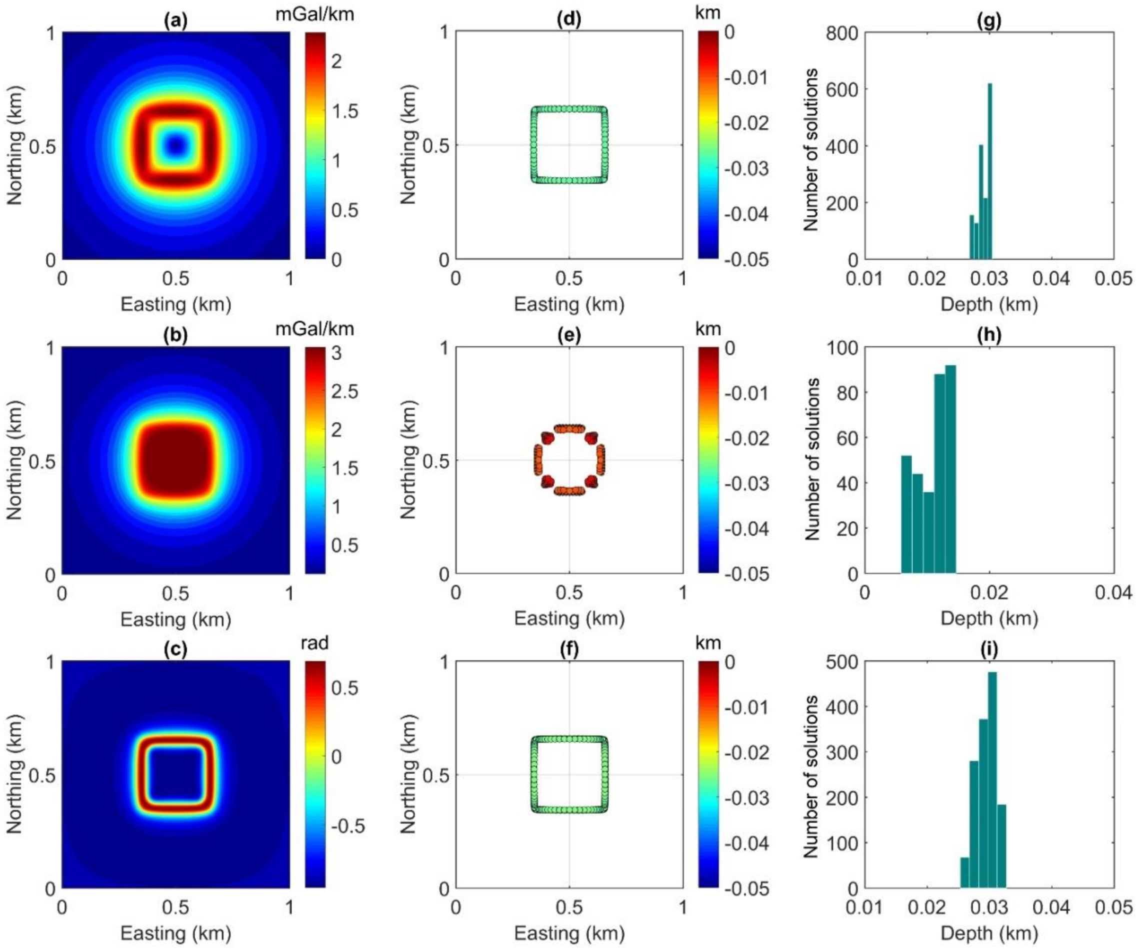

Figure 2. Results for the data in Fig. 1b: (a) THG, (b) TG, (c) THGED, (d) ED-THG, (e) ED-TG, (f) ED-THGED, (g) Histogram of the ED-THG solutions, (h) Histogram of the ED-TG solutions, (i) Histogram of the ED-THGED solutions

In the second one, we consider a more extensive scale model with geometric parameters listed in Table 1. This model includes two prismatic sources, A and B, with 200 and 120 kg/m^3 density contrasts, respectively. Figs. 3a and 3b depict the model and its gravity anomaly. Figs. 4a-c present the THG, TG, and THGED of the anomaly, respectively. We can see that the THG and THGED generate maximum values close to both bodies' actual edges. However, the TG does not provide the peaks over the edges of the body B. Like the first example, the Blakely and Simpson (1986) method was used to find the THG and TG peaks, and then the peak locations were used to select the windows for the ED-THG and ED-TG. Since the THGED creates balanced anomalies for the edges of the bodies located at different depths, a threshold value of 0.3 was used to detect the edge locations, as the first example. Figs. 4d-f present the depths estimated by the ED-THG, ED-TG, and ED-THGED, respectively. Figs. 4g-i depict the histograms of the ED-THG, ED-TG, and ED-THGED solutions. One can see that the ED-THG is effective in estimating the depth of body A, but it cannot determine all the locations and depths of body B. The ED-TG is less effective in mapping both bodies. The solutions from the proposed method ED-THGED show all the bodies closer to the actual depths than those estimated by the ED-THG and ED-TG.

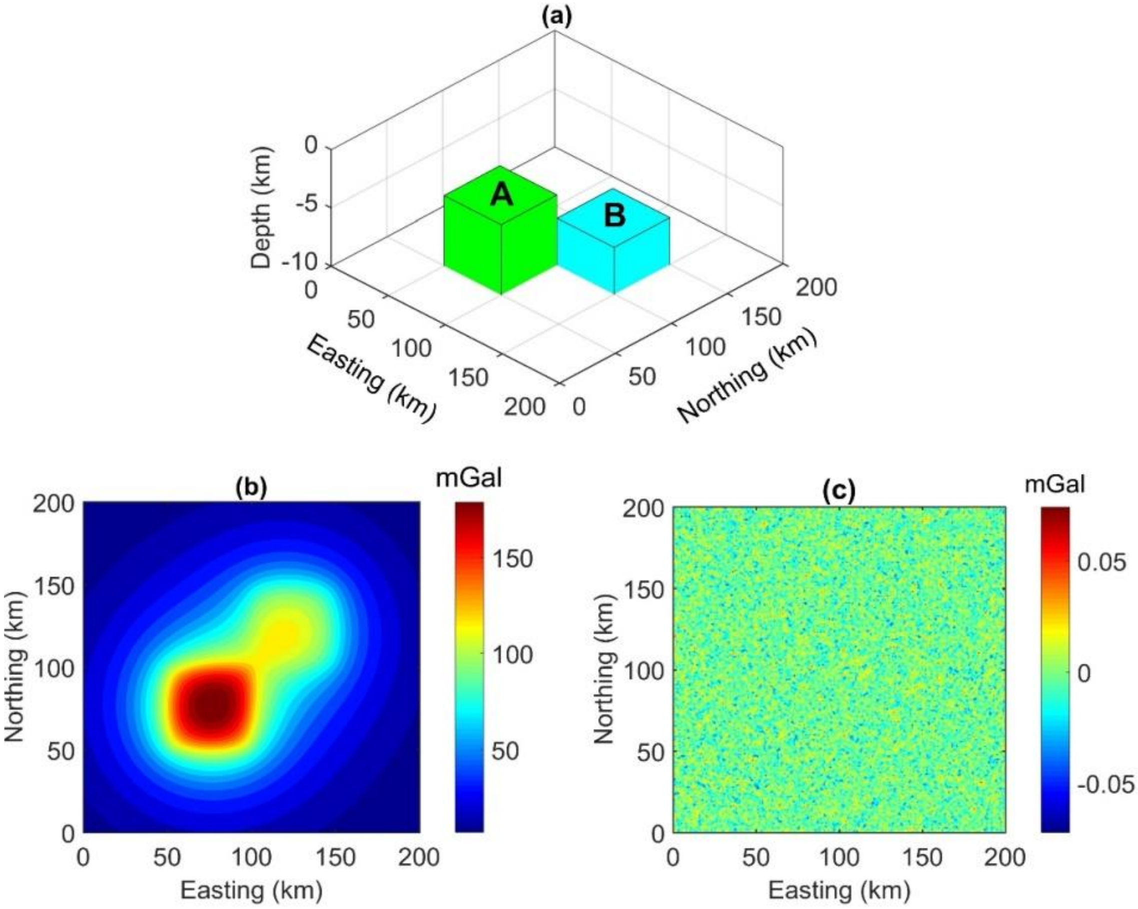

Figure 3. (a) The second model, (b) gravity anomaly of the model, (c) Gaussian noise

Table 1. Geometric parameters of the second model

Parameters	A	B
x-coordinate of center (km)	75	125
y-coordinate of center (km)	75	125
Width (km)	50	50
Length (km)	50	50
Top depth (km)	4	6

To test the stability of the ED-THGED technique, anomalies of Fig. 3b were contaminated with noise having an amplitude of 0.01% of anomaly maximum (Fig. 3c). Figs. 5a-c present the maps of the THG, TG, and THGED of noisy data. The peaks in the THG, TG, and THGED maps continue to be used in the Euler deconvolution methods. Figs. 5d-f depict the depths obtained from applying the ED-THG, ED-TG, and ED-THGED, respectively. The histograms of the ED-THG, ED-TG, and ED-THGED solutions are shown in Figs. 5g-i, respectively. In the presence of noise, many less significant peaks appear in the THG and TG outputs, bringing many spurious windows for the ED. Thus, the ED-THG and ED-TG generate many false solutions (Figs. 5d and e). In this case, the solution distribution in Fig. 5f suggests that the ED-THGED is less noise-sensitive than the ED-THG and ED-TG. The calculated depths from the ED-THGED are close to the actual values.

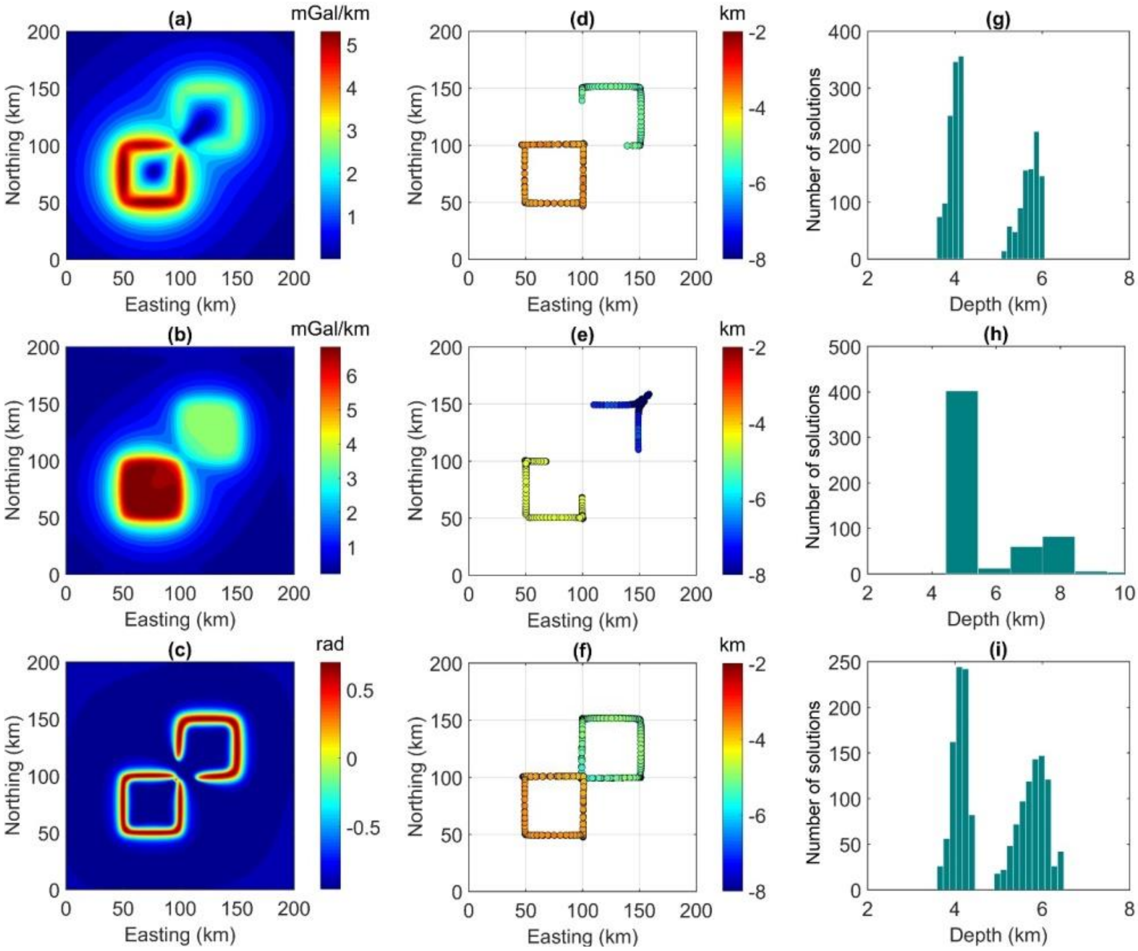

Figure 4. Results for the data in Fig. 3b: (a) THG, (b) TG, (c) THGED, (d) ED-THG, (e) ED-TG, (f) ED-THGED, (g) Histogram of the ED-THG solutions, (h) Histogram of the ED-TG solutions, (i) Histogram of the ED-THGED solutions

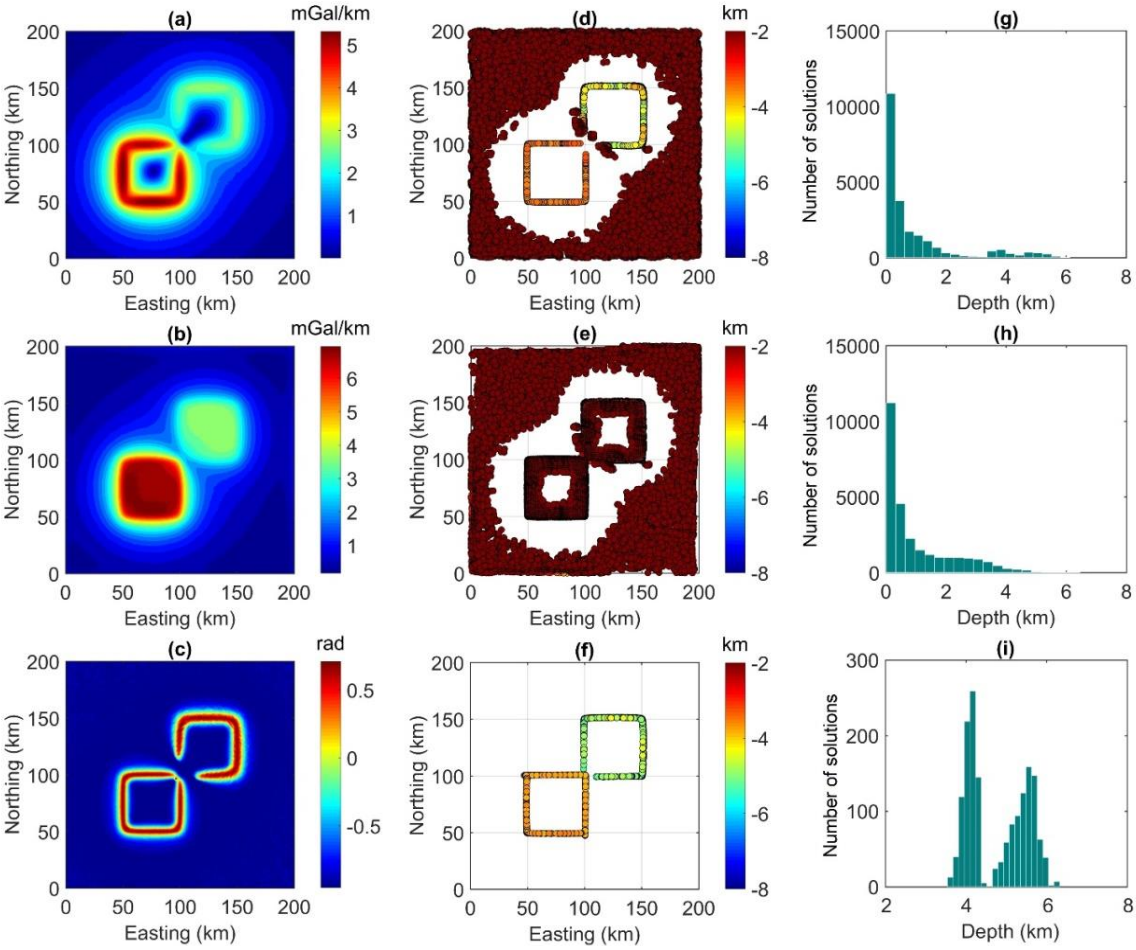

Figure 5. Results for the data in Fig. 3b after adding noise: (a) THG, (b) TG, (c) THGED, (d) ED-THG, (e) ED-TG, (f) ED-THGED, (g) Histogram of the ED-THG solutions, (h) Histogram of the ED-TG solutions, (i) Histogram of the ED-THGED solutions

3.2. Real applications

3.2.1. The Voisey's Bay Ni-Cu-Co deposit

The practical application of the proposed method ED-THGED was estimated by mapping the massive sulfide ore deposit from actual gravity data of Voisey's Bay, Canada. The Voisey's Bay Ni-Cu-Co deposit (Fig. 6) is one of Canada's most significant mineral discoveries in the 20th Century (Farquharson et al., 2008). The troctolite to gabbroic rocks host this deposit, which is emplaced along the tectonic contact between the Archean rocks of the Nain province and the Paleoproterozoic rocks of the Churchill province (Fig. 6). The deposit is not visible on the surface except for a small gossan (Wilton et al., 2021). Geophysical surveys and diamond drilling revealed the Void ore body buried under 20 meters of till (Wilton et al., 2021). Fig. 7 displays the Bouguer gravity data of the deposit after digitizing and interpolating into a regular grid with 20 ×24 grid points (King, 2007).

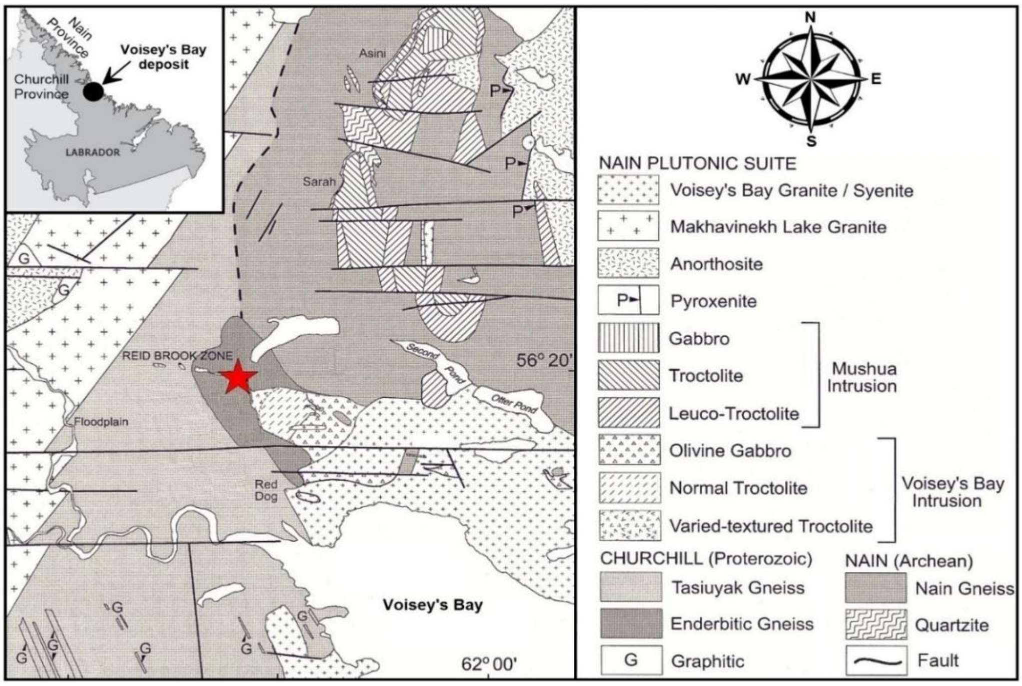

Figure 6. Geology map of the Voisey's Bay area showing the location of the Voisey's Bay Ni-Cu-Co deposit (red star) (Li and Naldrett, 1999)

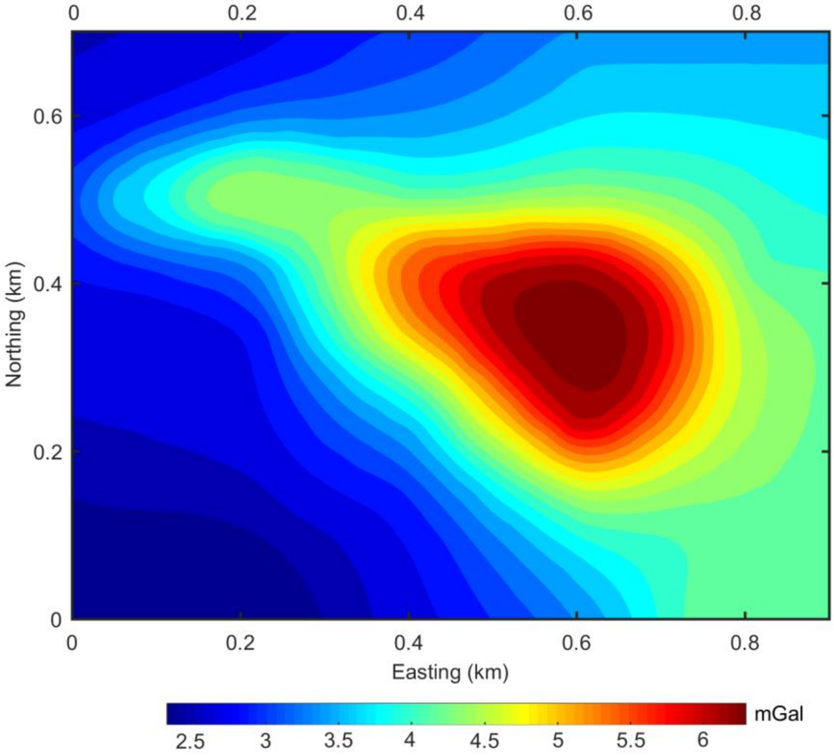

Figure 7. Bouguer data map over the Voisey's Bay Ni-Cu-Co deposit

Figs. 8a-c show the THG, TG, and THGED of anomalies in Fig. 7, respectively. The high amplitude anomalies dominate the THG and TG outputs, while the THGED can determine all edges more clearly. Figs. 8d-f show the results from applying the ED-THG, ED-TG, and ED-THGED to data in Fig. 7 and using the window locations determined by the maxima of the THG, TG, and THGED, respectively. The histograms of these results are shown in Figs. 8g-8i, respectively. We can see that the ED-THG and ED-TG results are noisy, especially since the ED-TG brings many spurious solutions. The presented method is less susceptible to noise than the ED-THG and ED-TG, and it can provide a more continuous body compared to other methods. Most of the depths from the ED-THGED method range from 10 to 30 m.

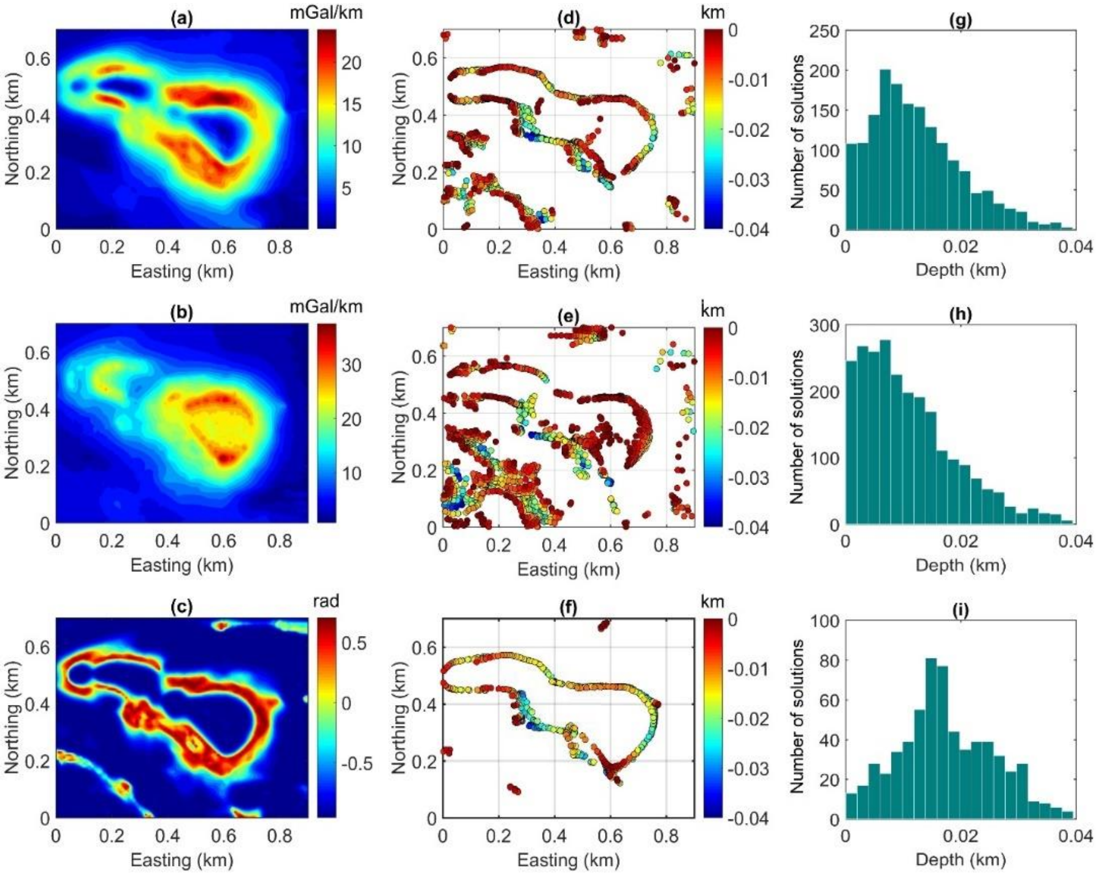

Figure 8. Results for the data in Fig. 7 (a) THG, (b) TG, (c) THGED, (d) ED-THG, (e) ED-TG, (f) ED-THGED, (g) Histogram of the ED-THG solutions, (h) Histogram of the ED-TG solutions, (i) Histogram of the ED-THGED solutions

3.2.2. The Hanoi basin

We further estimated the practical application of the improved algorithm ED-THGED by interpreting Bouguer anomalies from the Hanoi basin (Fig. 9). The region is between the Cenozoic Indochina block and the South China block in northern Vietnam. The region has over Quaternary sediments and some northwest-southeast trending faults (Koszowska et al., 2007; Phach et al., 2020). The gravity dataset of the basin was collected by the Geophysical Division of Vietnam and is displayed in Fig. 10.

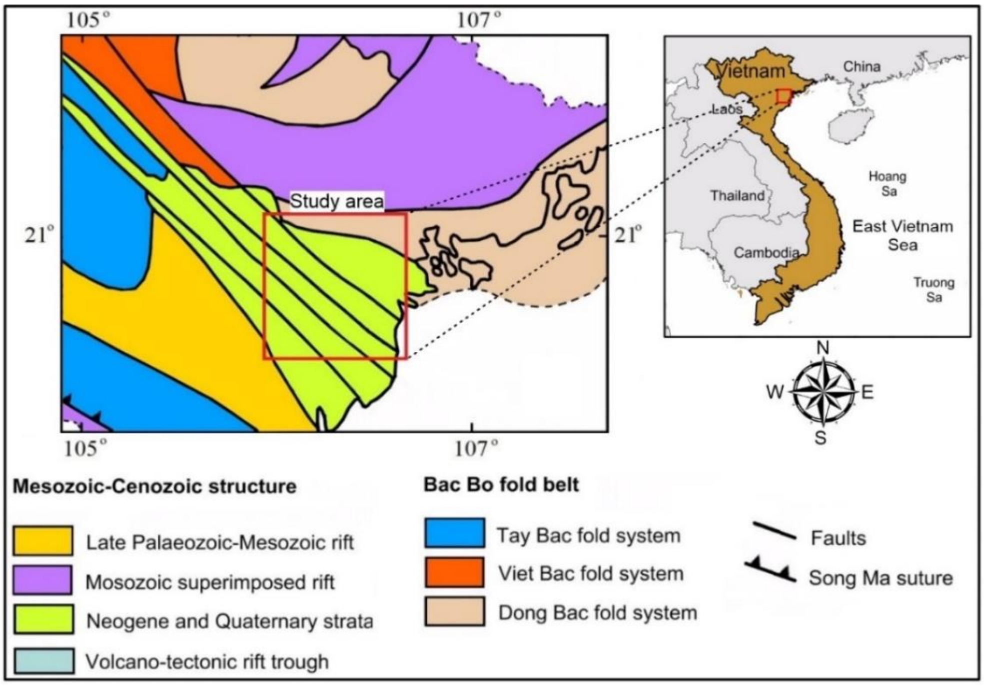

Figure 9. Geology map of Northeast Vietnam showing the location of the Hanoi basin (Koszowska et al., 2007)

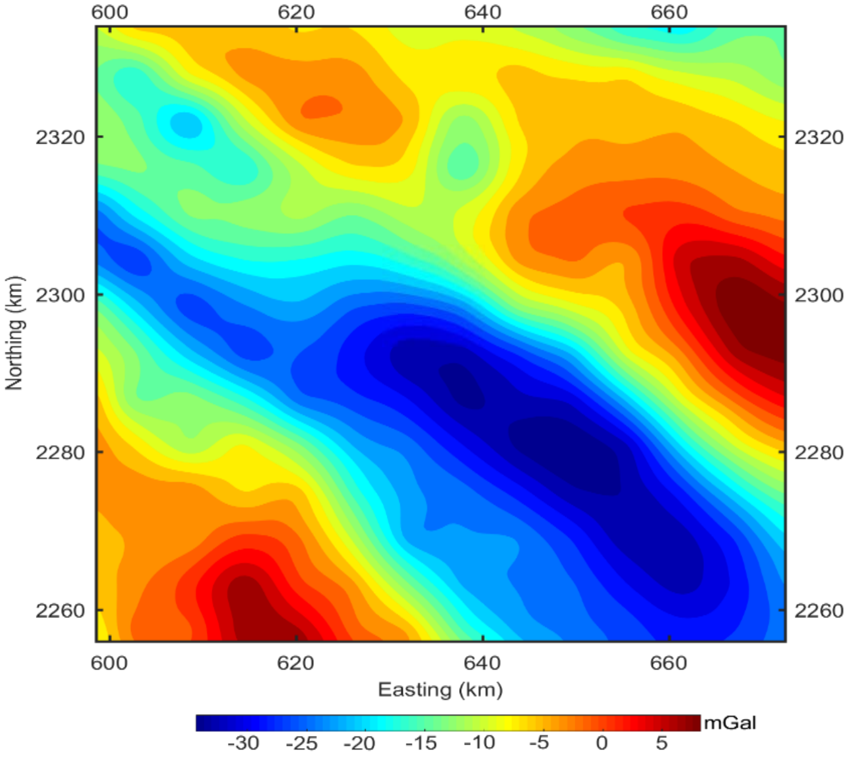

Figure 10. Bouguer data map of the Hanoi basin

Figures. 11a-c display the THG, TG, and THGED of Bouguer data in Fig. 10. The northwest-southeast trending structures dominate the THG, while isolated sources dominate the AS. Again, the THGED effectively determines all structures' boundaries with different anomalies. Using the window locations determined by the maxima of the THG, TG, and THGED, the depths of structures were computed by the ED-THG, ED-TG, and ED-THGED. Figs. 11d-f show the results of ED-THG, ED-TG, and ED-THGED. The histograms of these results are shown in Figs. 11g-11i, respectively. The determined structures from the ED-THG and ED-THGED are generally located at depths from 0.5 to 3.5 km, while most sources in the ED-TG map are less than 2 km. In this case, the ED-THGED still provides a continuous structure compared to other methods.

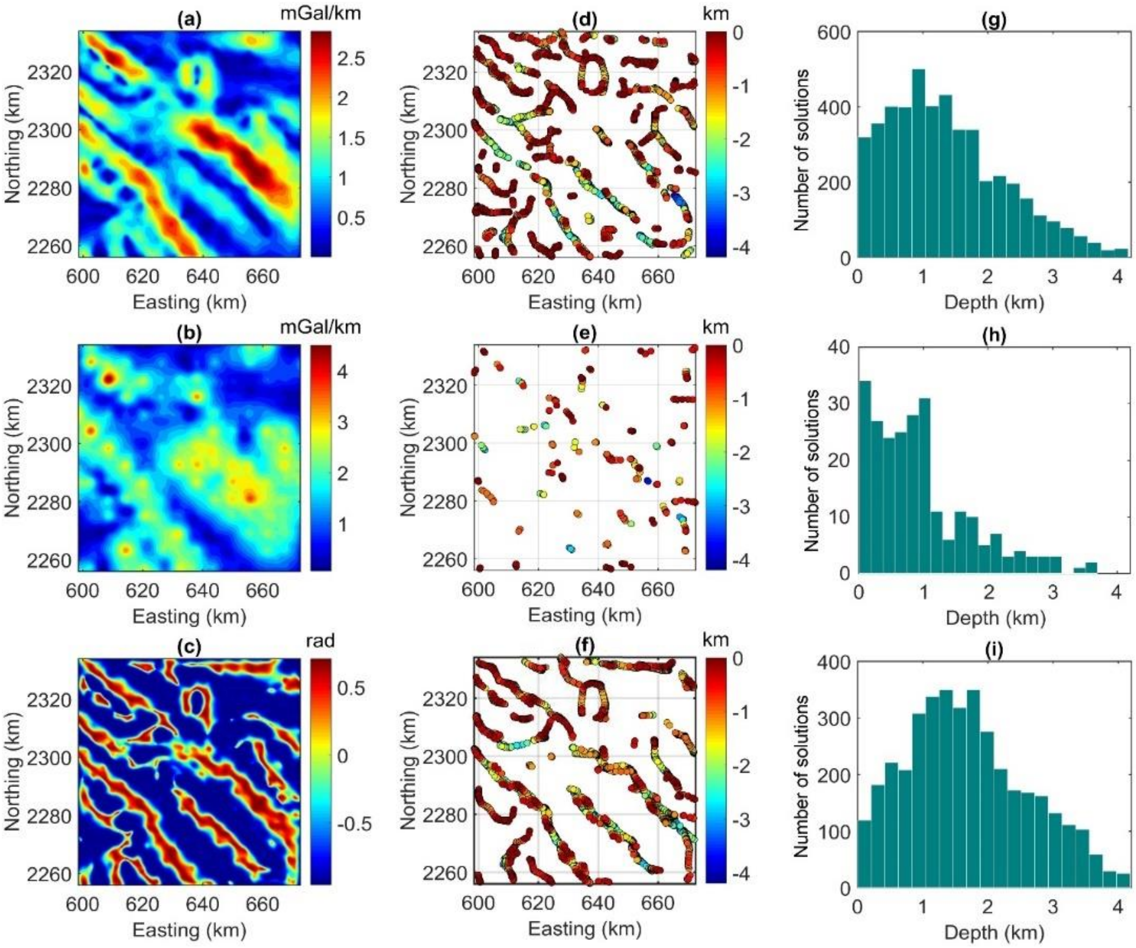

Figure 11. Results for the data in Fig. 10: (a) THG, (b) TG, (c) THGED, (d) ED-THG, (e) ED-TG, (f) ED-THGE, (g) Histogram of the ED-THG solutions, (h) Histogram of the ED-TG solutions, (i) Histogram of the ED-THGED solutions

4. Discussions

The first model with one prism is not affected by interference between anomalies. Hence the solutions obtained from the ED-THG and ED-TG methods are observed to converge at the body location, like the ED-

THGED. However, the ED-THG and ED-THGED bring better depth estimates than the ED-TG. The reason is that the use of the THG and THGED creates more accurate boundaries than the TG; hence, they bring better windows for the ED. In addition, we note that the solutions from the ED-THGED are closer to the actual depth than those estimated by the ED-THG. In the second model, the THG and TG are dominated by significant amplitude anomalies of the shallow body, as Kamto et al. (2023) and Alvandi et al. (2023) reported. For this reason, the ED-THG and ED-TG methods cannot determine all the source locations. Since the THGED produces balanced anomalies for the edges of the different bodies, the ED-THGED has an improved performance compared with the ED-THG and ED-TG. The noise in the third synthetic example generates many artifacts in the ED-THG and ED-TG maps. However, we can minimize the noise and detect density sources more precisely by using the vertical gradient calculated by the β-VDR and the window locations determined by the THGED maxima for the ED.

For a real example from the Voisey's Bay Ni-Cu-Co deposit, the ED-THGED performs better than the ED-THG and ED-TG. The ED-THGED result reveals the presence of a massive sulfide deposit in the region more clearly, which is known as an ovoid ore body as reported by some other authors (e.g., Huminicki et al., 2008; Farquharson et al., 2008; Lelievre et al., 2012). Most of the depths from the ED-THGED method range from 10 to 30 m, which agrees with the results from drill holes (i.e., Farquharson et al., 2008; Lelievre et al., 2012). In the second real example, the ED-THG does not provide continuous linear structures in the Hanoi basin since the maxima locations in the THG map are not entirely determined by the peak detection method (Pham et al., 2021). In addition, ED-THG brings more solutions than ED-THGED, which may relate to the noise issue, as reported in the model study. According to Paoletti et al. (2014), the TG often creates a single bell-shaped signal over the source center; hence, the structures determined by the ED-TG are discontinuous. The ED-THGED helps map a wide range of density boundaries of the Hanoi basin. These structures correlate well with northwest-southeast trending faults in the Hanoi basin. The solutions of the ED-THGED also agree very well with the lineaments of previous gravity studies (i.e., Son et al., 2005 and Pham et al., 2021) using the peak detection technique. The determined structures are generally located at depths from 0.5 to 3.5 km (Fig. 11f), obscured by the basin's sedimentary rocks. This agrees with the results reported by Son et al. (2005), which showed that most of the source depths in the basin are less than 3.5 km. By comparing the findings in Fig. 11, we can say that the ED-THGED method can determine more density structures than the ED-THG and ED-TG. The ED-THGED generates more continuous linear northwest-southeast trending structures that can be utilized to enhance the current geology map. Although we did not focus on geological and tectonic interpretations of the Hanoi basin, the result obtained from the improved method ED-THGED can be helpful for further studies on the geology and tectonics of this basin.

5. Conclusions

We have improved the ED algorithm for the gravity case by using the vertical gradient calculated from the β-VDR technique and the window detected from the maxima of the THGED. We compared the presented technique (ED-THGED) with other ED methods based on the THG (ED-THG) and TG (ED-TG) and showed that the ED-THGED could provide structure locations more clearly and with higher precision. In addition, the synthetic examples showed that the proposed algorithm is less susceptible to noise and does not provide spurious solutions. The ED-THGED was applied to interpret real datasets from the Voisey's Bay deposit and the Hanoi basin. Our findings showed that the proposed method is effective in clearly mapping the deposits and structures that are obscured by sedimentary rocks.

Acknowledgments

This research is funded by Vietnam National Foundation for Science and Technology Development (NAFOSTED) under grant number 105.05-2021.53. It has been also supported by CNPq, Brazil, Grant Number 316376/2021-3. Ngo Thi To Nhu was funded by the Master, PhD Scholarship Programme of Vingroup Innovation Foundation (VINIF), code VINIF.2023.ThS.101.

References

Alamdar K., Kamkare-Rouhani A., Ansari A.H., 2015. Interpretation of the magnetic data from anomaly 2c of Soork iron ore using the combination of the Euler deconvolution and TDX filter. Arab J. Geosci., 8, 6021–6035.

Alvandi A., Ardestani V.E., 2023. Edge detection of potential field anomalies using the Gompertz function as a high-resolution edge enhancement filter. Bull. Geophys. Oceanogr., 64(3), 279–300.

Alvandi A., Ghanati R., 2023. Using magnetic data for estimating the location of lateral boundaries and the depth of the shallow salt dome of Aji-Chai, East Azerbaijan Province, Iran. Int. J. Min. Geo-Eng., 57(3), 251–258.

Alvandi A., Su K., Ai H., Ardestani V.E., Lyu C., 2023. Enhancement of Potential Field Source Boundaries Using the Hyperbolic Domain (Gudermannian Function). Minerals, 13, 1312.

Aprina P.U., Santoso D., Alawiyah S., Prasetyo N., Ibrahim K., 2024. Delineating geological structure utilizing integration of remote sensing and gravity data: a study from Halmahera, North Molucca, Indonesia. Vietnam J. Earth Sci., 46(2), 147–68.

Barbosa V.C.F., Silva J.B.C., Medeiros W.E., 1999. Stability analysis and improvement of structural index estimation in Euler deconvolution. Geophysics, 64(1), 48–60.

Beiki M., 2010. Analytic signals of gravity gradient tensor and their application to estimate source location. Geophysics, 75(6), I59–174.

Blakely R., Simpson R., 1986. Approximating edges of source bodies from magnetic or gravity anomalies. Geophysics, 51(7), 1494–1498.

Catalán M., Martín Davila J., 2003. A magnetic anomaly study offshore the Canary Archipelago. Mar. Geophys. Res., 24(1), 129–148.

Castro F.R., Oliveira S.P., de Souza J., Ferreira F.J.F., 2018. Combining tilt derivative filters: New approaches to enhance magnetic anomalies. Rev. Bras. Geofis., 36(3), 335–343.

Castro F.R., Oliveira S.P., de Souza J., Ferreira F.J.F., 2020. Constraining Euler deconvolution solutions through combined tilt derivative filters. Pure Appl. Geophys., 177(10), 4883–4895.

Chen Q., Dong Y., Cheng S., Han L., Xu H., Chen H., 2014. Interpretation of fault system in the Tana Sag, Kenya, using edge recognition techniques and Euler deconvolution. J. Appl. Geophys., 109, 150–161.

Cooper G.R.J., 2004. Euler deconvolution applied to potential field gradients. Explor. Geophys., 35(3), 165–170.

Cordell L., 1979. Gravimetric expression of graben faulting in Santa Fe Country and the Espanola Basin. In 30th Field Conference New Mexico. New Mexico Geological Society Guidebook; New Mexico Geological Society: Socorro, NM, USA, 59–64.

Ekinci Y.L., Balkaya Ç., Şeren A., Kaya M.A., Lightfoot C.S., 2014. Geomagnetic and geoelectrical prospection for buried archaeological remains on the Upper City of Amorium, a Byzantine city in midwestern Turkey. J. Geophys. Eng., 11(1), 015012.

Ekinci Y.L., Ertekin C., Yiğitbaş E., 2013. On the effectiveness of directional derivative based filters on gravity anomalies for source edge approximation: synthetic simulations and a case study from the Aegean graben system (Western Anatolia, Turkey). J Geophys. Eng., 10(3), 035005.

Ekinci Y.L., Yiğitbaş E., 2012. A geophysical approach to the igneous rocks in the Biga Peninsula (NW

Turkey) based on airborne magnetic anomalies: Geological implications. Geodin. Acta, 25, 267–285.

Ekinci Y.L., Yiğitbaş E., 2015. Interpretation of gravity anomalies to delineate some structural features of Biga and Gelibolu peninsulas, and their surroundings (northwest Turkey). Geodin. Acta, 27(4), 300–319.

El Gout R., Khattach D., Houari M.R., Kaufmann O., Aqil H., 2010. Main structural lineaments of north-eastern Morocco derived from gravity and aeromagnetic data. J. Afr. Earth Sci., 58(2), 255–271.

EL Badrawy H.T., Araffa S.A.S., Gabr A.F., 2021. Application of the multi-potential geophysical techniques for groundwater evaluation in a part of Central Sinai Peninsula, Egypt. Acta Geodyn. Geomater, 18(1), 61–70.

Fairhead J.D., Bennett K.J., Gordon D.R.H., Huang D., 1994. Euler: Beyond the "black box". In 64th Annual International Meeting. Expanded Abstracts. SEG, 422–424.

Farquharson C.G., M.R Ash., H.G. Miller., 2008. Geologically constrained gravity inversion for the Voisey's Bay ovoid deposit. The Lead. Edge, 27(1), 64–69.

Florio G., Fedi M., Pašteka R., 2006. On the application of Euler deconvolution to the analytic signal. Geophysics, 71(6), L87SEGL93.

Ganguli S.S., Pal S.K., Sundaralingam K., Kumar P., 2021. Insights into the crustal architecture from the analysis of gravity and magnetic data across Salem-Attur Shear Zone (SASZ), Southern Granulite Terrane (SGT), India: an evidence of accretional tectonics. Episodes, 44, 419SEG442.

Huang L., Zhang H., Li C.F., Feng J., 2022. Ratio-Euler deconvolution and its applications. Geophys. Prospect., 70(6), 1016–1032.

Huminicki M.A.E., P.J. Sylvester, R. Lastra, L.J. Cabri D., Evans-Lamswood D., D.H.C. Wilton, 2008. First report of platinum-group minerals from a hornblende gabbro dyke in the vicinity of the Southeast Extension Zone of the Voisey's Bay Ni-Cu-Co deposit, Labrador. Mineral. Petrol., 92(1–2), 129–164.

Jekeli C., 2009. On methods to select solutions in Euler deconvolution of gravitation and gradient measurements: Stud. Geophys. Geod., 53, 443–457.

Jorge V.T., Oliveira S.P., Pham L.T., Duong V.H.A., 2023. balanced edge detector for aeromagnetic data. Vietnam J. Earth Sci., 45(3), 326–37.

Kafadar O., Oksum E., 2024. Enhanced dip angle map using Kuwahara and Gaussian filters: an example from Burdur region, Türkiye. Turk. J. Earth Sci., 33(4), 395-406.

Kamto P.G., Oksum E., Pham L.T., Kamguia J., 2023. Contribution of advanced edge detection filters for the structural mapping of the Douala Sedimentary Basin along the Gulf of Guinea. Vietnam J. Earth Sci., 45(3), 287–302.

King A., 2007. Review of Geophysical Technology for Ni.-. Cu.-. PGE. deposits, in "Proceedings of Exploration 07: Fifth Decennial International Conference on Mineral Exploration" edited by B. Milkereit, 647–665.

Koszowska E., Wolska A., Zuchiewicz W., Cuong N.Q., Pecskay Z., 2007. Crustal contamination of Late Neogene basalts in the Dien Bien Phu Basin, NW Vietnam: some insights from petrological and geochronological studies. J. Asian Earth Sci., 29(1), 1–17.

Kumar U., Pal S.K., Sahoo S.D., Narayan S., Saurabh Mondal S., Ganguli S.S., 2018. Lineament mapping over Sir Creek offshore and its surroundings using high resolution EGM2008 Gravity data: an integrated derivative approach. J. Geol Soc India., 91, 671–678.

Kumar U., Narayan S., Pal S.K., 2020. Structural and tectonic interpretation of EGM2008 gravity data around the Laccadive ridge in the Western Indian Ocean: an implication to continental crust. Geocarto Int., 37(11), 3179–3198.

Kumar U., Narayan S., Pal S.K., 2022. Structural and tectonic interpretation of EGM2008 gravity data around the Laccadive ridge in the Western Indian Ocean: an implication to continental crust. Geocarto Int., 37(11), 3179–3198.

Lelievre P.G., C.G. Farquharson, C.A. Hurich, 2012. Joint inversion of seismic traveltimes and gravity data on unstructured grids with application to mineral exploration. Geophysics, 77(1), K1–K15.

Li C., Naldrett A.J., 1999. Geology and petrology of the Voisey's Bay intrusion: reaction of olivine with sulfide and silicate liquids. Lithos, 47(1-2), 1–31.

Marson I., Klingele E.E., 1993. Advantages of using the vertical gradient of gravity for 3-D interpretation. Geophysics, 58(11), 1588–1595.

Melo F.F., Barbosa V.C.F., 2020. Reliable Euler deconvolution estimates throughout the vertical derivatives of the total-field anomaly. Comput Geosc., 138, 104436.

Melouah O., Ebong E.D., Abdelrahman K., Eldosouky A.M., 2023. Lithospheric structural dynamics and geothermal modeling of the Western Arabian Shield. Sci. Rep., 13, 11764.

Narayan, S., Sahoo S.D., Pal S.K., Kumar U., Pathak V.K., Majumdar T.J., Chouhan A., 2016. Delineation of structural features over a part of the Bay of Bengal using total and balanced horizontal derivative techniques. Geocarto Int., 32, 351–366.

Narayan S., Kumar U., Pal S.K., Sahoo S.D., 2021. New insights into the structural and tectonic settings of the Bay of Bengal using high-resolution earth gravity model data. Acta Geophys., 69, 2011–2033.

Nasuti Y., Nasuti A., Moghadas D. 2019. STDR: a novel approach for enhancing and edge detection of potential field data. Pure Appl. Geophys., 176(2), 827–841.

Oliveira S.P., Pham L.T., 2022. A stable finite difference method based on upward continuation to evaluate vertical derivatives of potential field data. Pure Appl. Geophys., 179(12), 4555–4566.

Oliveira S.P., Bongiolo A.deB.eS., Pham L.T., DE Castro L.G., Jorge V.T., 2023. On the practical implementation of the enhanced horizontal derivative filter for potential field data. Contrib. Geophys. Geod., 53(4), 319–331.

Pal S.K., Majumdar T.J., Pathak V.K., Narayan S., Kumar U., Goswami O.P., 2016a. Utilization of high-resolution EGM2008 gravity data for geological exploration over the Singhbhum-Orissa Craton, India. Geocarto Int., 31(7), 783–802.

Pal S.K., Narayan S., Majumdar T.J., Kumar U., 2016b. Structural mapping over the 85°E Ridge and surroundings using EIGEN6C4 high resolution global combined gravity field model: an integrated approach. Mar. Geophys. Res., 37(3), 159–184.

Paoletti V., Fedi M., Florio G., Supper R., Rapolla A., 2004. The new integrated aeromagnetic map of the Phlegrean Fields volcano and surrounding areas. Ann. Geophys., 47(5), 1569–1580.

Pašteka R., Richter P., 2005. Improvement of the Euler deconvolution algorithm by means of the introduction of regularized derivatives. Contrib. Geophys. Geod., 35(1), 1–18.

Pašteka R., Kušnirák D., 2020. Role of Euler Deconvolution in Near Surface Gravity and Magnetic Applications. In: Biswas A, Sharma SP, editors. Advances in Modeling and Interpretation in Near Surface Geophysics. Cham: Springer, 223–262.

Phach P.V., Lai V.C., Shakirov R.B., Le D.A., Tung D.X., 2020. Tectonic activities and evolution of the Red River Delta (North Viet Nam) in the Holocene. Geotecton, 54(1), 113–129.

Pham L.T., Kafadar O., Oksum E., Hoang Minh T., 2021. A comparative study on the peak detection methods used to interpret potential field data: a case study from Vietnam, Geocarto Int., 37(13), 3679–3696.

Pham L.T., 2023. A novel approach for enhancing potential fields: application to aeromagnetic data of the Tuangiao, Vietnam. Eur., Phys., J. Plus, 138(12), 1134.

Pham L.T., 2024a. An improved edge detector for interpreting potential field data. Earth Sci., Inform, 17, 2763–2774.

Pham L.T., 2024b. A stable method for detecting the edges of potential field sources. IEEE Trans. Geosci., Remote Sens., 62, 5912107.

Pham L.T., 2024c. Mapping the structural configuration of the northern part of the Central Indian Ridge from satellite gravity data using derivatives of the horizontal gradient. Advances in Space Research. https://doi.org/10.1016/j.asr.2024.05.054.

Pham L.T., Prasad K.N.D., 2023. Analysis of gravity data for extracting structural features of the northern region of the Central Indian Ridge. Vietnam J. Earth Sci., 45(2),147–63.

Pham L.T., Oliveira S.P., Abdelrahman K., Gomez-Ortiz D., Nguyen D.V., Vo Q.T., Eldosouky A.M., 2024a. Selection of Euler deconvolution solutions using the enhanced horizontal gradient and stable vertical differentiation. Open Geosci., 16(1), 20220637.

Pham L.T., Duong H.V., Kieu Duy T., Oliveira S.P., Lai G.M., Bui T.M., Oksum E., 2024b. An effective edge detection technique for subsurface structural mapping from potential field data. Acta Geophys., 72, 1661–1674.

Reid A.B., Allsop J.M., Granser H., Millett A.J., Somerton I.W., 1990. Magnetic interpretation in three dimensions using Euler deconvolution. Geophysics, 55(1), 80–91.

Reid A.B., FitzGerald D., McInerny P., 2003. Euler deconvolution of gravity data. SEG Technical Program Expanded Abstracts, 80–583.

Reid A.B., Ebbing J., Webb S.J., 2014. Avoidable Euler errors - the use and abuse of Euler deconvolution applied to potential fields. Geophys. Prospect., 62(5), 1162–1168.

Roest W.R.J., Verhoef J., Pilkington M., 1992. Magnetic interpretation using the 3-D analytic signal. Geophysics, 57(1), 116–125.

Ruppel A., Jacobs J., Eagles G., Läufer A., Jokat W., 2018. New geophysical data from a key region in East Antarctica: Estimates for the spatial extent of the Tonian Oceanic Arc Super Terrane (TOAST). Gondwana Res., 59, 97–107.

Saadi N.M., Aboud E., Saibi H., Watanabe K., 2008. Integrating data from remote sensing, geology and gravity for geological investigation in the Tarhunah area, Northwest Libya, Int. J. Digit. Earth, 1(4), 347–366.

Sahoo S., Narayan S., Pal S.K., 2022a. Fractal analysis of lineaments using CryoSat-2 and Jason-1 satellite-derived gravity data: Evidence of a uniform tectonic activity over the middle part of the Central Indian Ridge. Phys. Chem. Earth, 128, 103237.

Sahoo S., Narayan S., Pal S.K., 2022b. Appraisal of gravity-based lineaments around Central Indian Ridge (CIR) in different geological periods: Evidence of frequent ridge jumps in the southern block of CIR. J. Asian Earth Sci., 239, 105393.

Son V.T., Minh L.H., Hung L.V., 2005. Determining the horizontal position and depth of the density discontinuities in the Red Revier Delta by using the vertical derivative and Euler deconvolution for the gravity anomaly data. Geol. J., 287, 39–52 (in Vietnamese).

Thompson D.T., 1982. EULDPH: A new technique for making computer-assisted depth estimates from magnetic data. Geophysics, 47(1), 31–37.

Wilton D.H.C., G.M. Thompson, D., Evans Lamswood, 2021. MLA-SEM Characterization of Sulphide Weathering, Erosion, and Transport at the Voisey's Bay Orthomagmatic Ni-Cu-Co Sulphide Mineralization, Labrador, Canada. Minerals, 11, 1224.

Zhang C., Mushayandebvu M.F., Reid A.B., Fairhead J.D., Odegard M.E., 2000. Euler deconvolution of gravity tensor gradient data. Geophysics, 65, 512–520.

Zhang J., Zhao G., Shen W., Li S., Sun M., 2015. Aeromagnetic study of the Hengshan-WutaiFuping region: Unraveling a crustal profile of the Paleoproterozoic Trans-North China Orogen. Tectonophysics, 662, 208–218.